

Design Methodology of N-path Filters with Adjustable Frequency, Bandwidth, and Filter Shape

M. Naimul Hasan, *Student Member, IEEE*, Shahrokh Saeedi, *Member, IEEE*, Qun Jane Gu, *Senior Member, IEEE*, Hjalti H. Sigmarsson, *Member, IEEE*, and Xiaoguang “Leo” Liu, *Member, IEEE*

Abstract—In this paper, an adaptive N-path filter design technique is presented. The filter designed by this method can be reconfigured to different shapes, e.g. Butterworth or Chebyshev with variable bandwidth, based on the user requirements. In addition, an analytical synthesis procedure is introduced to realize high-order bandpass filters based on N-path architecture with a prescribed set of specifications. A proof-of-concept bandpass filter is fabricated and measured in a 65-nm CMOS process. The filter can be reconfigured to realize different filter shapes by changing coupling capacitors. The bandwidth of the proposed filter is also tunable. The passband of the filter is tunable from 0.2 GHz to 1.2 GHz with a gain of 14.5–18 dB, a noise figure of 3.7–5.5 dB, and a total power consumption of 37.5–52.7 mW. The channel bandwidth can be varied from 20 MHz to 40 MHz and the filter out-of-band IIP3 ($\Delta f=50$ MHz) is 25 dBm.

Index Terms—Bandpass filter, CMOS, impedance transformation, N-path, reconfigurable, synthesis, tunable bandwidth, tunable filter

I. INTRODUCTION

MODERN wireless communication standards, such as Long-time evolution (LTE) and the upcoming 5G standards, are supporting more and more frequency bands worldwide. To prevent strong transmit (TX) signals to desensitize the receiver (RX), electro-acoustic filters, such as surface acoustic wave (SAW), and bulk acoustic wave (BAW) filters, are usually used to isolate the TX and RX front-end circuits. As more frequency bands are supported, the number of SAW/BAW filters grow substantially. This situation is exacerbated by “carrier aggregation”, in which multiple adjacent or non-adjacent channels can be joined together to increase the data rate and bandwidth efficiency [1].

A straightforward approach is to integrate multiple narrow-band receivers, each with an independent frequency synthesizer and baseband chains. However, it is desirable to develop an architecture to reduce this multiplicity, and hence reduce area and decrease form factor. It may also be desirable to build up a reconfigurable system based on the allocation of frequency bands. Reconfigurable RF front-end filter/receiver

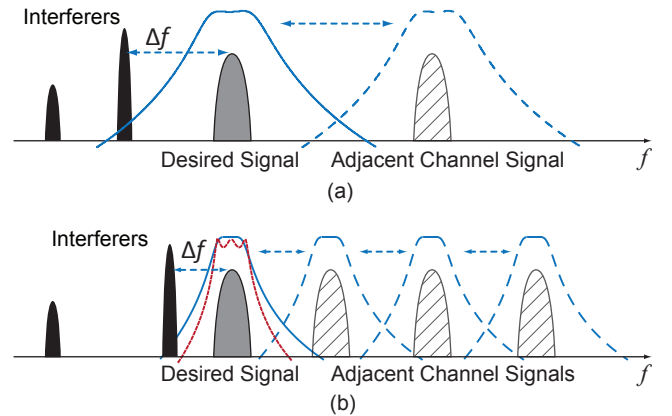


Fig. 1. Proposed tunable filter with capability of handling dynamic adverse and/or friendly interferers where rejection, gain, noise, and in-band group delay are traded off for optimal system performance. (a) Less occupied spectrum with far blocker. (b) Densely occupied spectrum with close blocker. A filter with higher roll-off can be utilized with the degradation of passband ripple. The blue curve resembles a Butterworth response while the red curve corresponds to a Chebyshev response with a 3 dB passband ripple.

[2]–[5] has also become attractive for software-defined radio applications. On the other hand, the signal bandwidth of modern wireless communication standards are becoming increasingly large. For example, with intra-band carrier aggregation, signal bandwidth of multiples of 20 MHz may be required. As a consequence, the in-band frequency response of the front-end filters, particularly in terms of gain flatness and group delay variation, becomes as important as the out-of-band rejection. Non-linear behavior of the front-end filters can also contribute to the non-linearity of the whole system. Passive coupled switched capacitor resonator based RF front-end filters are presented in [6], [7] to achieve high out-of-band linearity.

In the presence of dynamic interferers (blockers), a tunable filter offers flexible front-end filtering characteristics. In particular, being able to dynamically change the filtering response of the filter allows for the best trade-off between rejection and loss/noise. Fig. 1 shows such a scenario. If the frequency difference (Δf) between the desired signal and the unwanted out-of-band interference/blocker is large (Fig. 1(a)), a flat passband, wideband filter shape may be suitable for this application. If Δf is small, however, a narrowband filter shape with high stopband rejection is more appropriate to significantly suppress the blocker, albeit at the cost of slightly higher insertion loss.

Manuscript received June 30, 2017.

This work was supported by the National Science Foundation, EECS Award#:1444086.

M. Naimul Hasan was with the Department of Electrical and Computer Engineering, University of California at Davis, Davis, CA 95616 USA. He is now with Skywork Solutions, San Jose, CA 95134 USA.

Qun Jane Gu and Xiaoguang Liu are with the Department of Electrical and Computer Engineering, University of California, Davis, CA 95616, USA.

Shahrokh Saeedi and Hjalti Sigmarsson are with the Advanced Radar Research Center and the School of Electrical and Computer Engineering, University of Oklahoma, Norman, OK 73019, USA.

N-path filters have garnered significant research interest in recent years due to their capability to achieve high quality factor (Q), typically greater than 100, and wide frequency tuning range in integrated circuit technologies. Previous research on N-path based filters and receivers has been focused on realizing low-loss passband and steep rejection profiles to minimize in-band noise figure (NF) and increase the in-band (IB) /out-of-band (OOB) linearity. For example, in [8], a 6th order N-path filter is presented with 25 dB gain and 26 dBm OOB linearity. Various on-chip techniques have been presented in [5], [6], [9]–[11] to handle large OOB blockers. However, previous work on N-path tunable filters has not presented systematic design methodologies for realizing higher-order filter according to a set of prescribed specifications.

To this end, this paper presents, for the first time, methodology for designing high-order active RF front-end filters implemented with N-path technologies. An analytical synthesis procedure is introduced to realize high-order bandpass filter responses with a set of prescribed specifications such as type of filter approximation, passband ripple, out-of-band rejection, and in-band group delay. To demonstrate the effectiveness of this methodology, a fully tunable N-path filter with adjustable center frequency, bandwidth, and filter shape is also presented. The proposed design methodology will enable the design of high-performance integrated active filters for future wireless communication systems.

II. SYNTHESIS METHODOLOGY OF HIGHER-ORDER N-PATH FILTERS

A. Review of N-path Filters

Fig. 2(a) shows a regular, coupled-resonator, 3-pole bandpass (BP) filter implemented using gyrators. Fig. 2(b) shows the corresponding N-path implementation, where the resonators are replaced by switched capacitors. An N-path filter resembles a LC tank with a tunable center frequency and constant bandwidth [12]–[14]. In an N-path bandpass filter, the radio frequency (RF) signal is first downconverted to baseband, filtered by a lowpass filter, usually implemented with shunt capacitors, and then upconverted back to RF. This process effectively frequency shifts the lowpass frequency response to the RF frequency, creating a bandpass response. Similarly, a bandstop response can be created by highpass filtering of the downconverted RF signal using series connected capacitors. To preserve the impedance profile during the frequency translation process, a switch-based passive mixer is typically used [4], [10], [15]. If the output of the filter is taken directly from the baseband capacitors, i.e. without upconverting the downconverted signal back to RF, a receiver with integrated front-end filtering may also be realized [2], [4], [15]–[20].

The negative transconductance in the feedback path of the first stage increases the NF as it directly feeds back noise to the input port. The NF of the filter with clock frequency of 1 GHz for a regular implementation and decoupling the first stage (removing the $-g_{m1}$) is shown in Fig. 3. It is possible to achieve 5 dB lower NF by decoupling the first stage. The power consumption also reduces due to the removal of $-g_{m1}$.

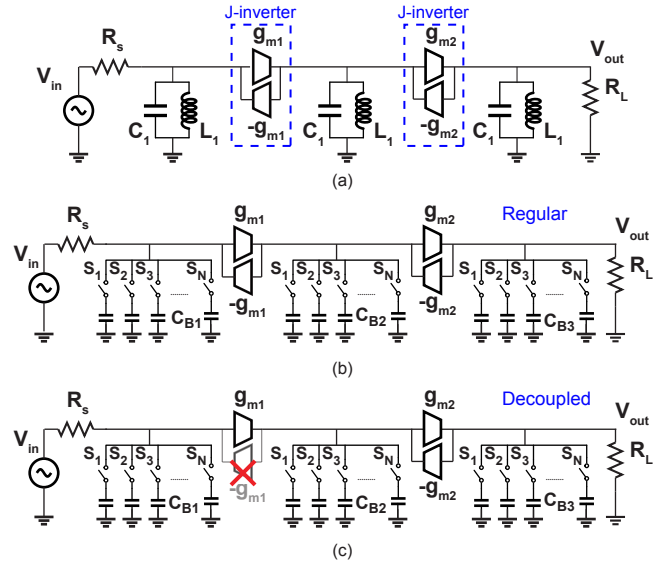


Fig. 2. Configuration of an N-path integrated BPF. (a) Coupled-resonator 3-pole BPF. (b) N-path implementation of the BPF. (c) BPF with the first stage decoupled using a single g_m cell.

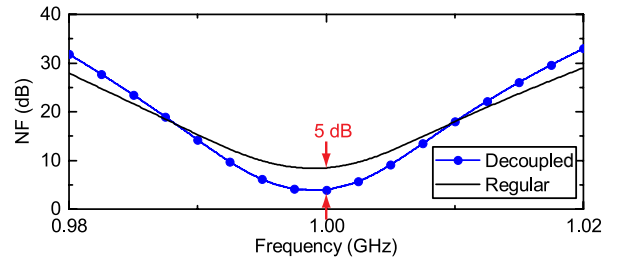


Fig. 3. The noise figure of the filter with and without decoupling the negative g_m cell in the first stage at $f_0 = 1$ GHz. $C_{B1} = C_{B3} = 32.24$ pF, $C_{B2} = 4$ pF, $g_{m1} = 14.14$ mS, $g_{m2} = 10$ mS and $g_{m3} = 5$ mS are considered in the simulation.

Therefore, to increase the gain, reduce the NF, and increase the dynamic range of the filter, the first gyrator is replaced with a single g_m cell (amplifier) as shown in Fig. 2(c) [8]. This effectively transforms the 3-pole bandpass filter prototype to a cascade of a 1-pole filter with a 2-pole filter. The OOB roll-off of the BPF still follows a 3-pole characteristic due to the impedance isolation by g_{m1} .

However, simply removing the feedback g_{m1} , alters the bandwidth of the filter as well as the desired filter shape as shown in Fig. 4. As a result, a proper synthesis procedure is required to realize the filter with desired bandwidth and passband shape while removing the negative g_m cell in the first stage. A similar technique for decoupling the first stage is also showed in [8] to reduce the power consumption as well as to reduce NF. However, due to the lack of a proper synthesis procedure of the filter, an extra feedback capacitor is used between input and output to maintain the passband ripple to a certain extent, which introduces stability concern in the filter. In the next section, the proper synthesis procedure will be discussed.

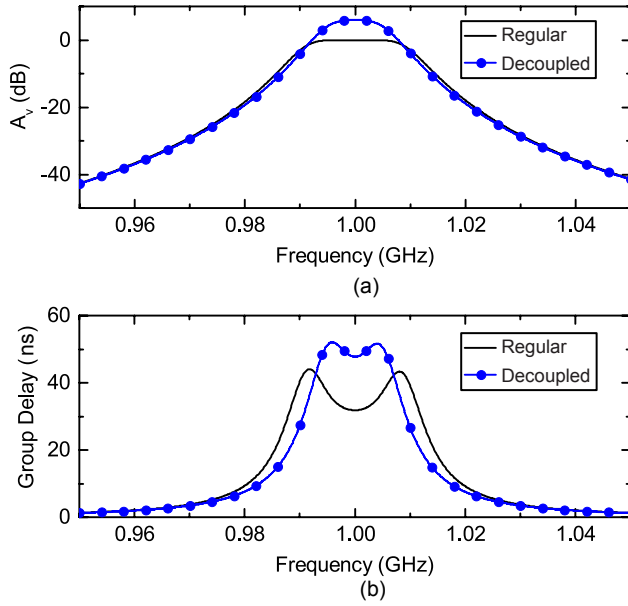


Fig. 4. Distortion in BPF response by simply removing the feedback g_{m1} . (a) Magnitude response of regular and decoupled bandpass filter. (b) Corresponding group delay.

B. Synthesis of first-stage-decoupled N -path filters

In general, any lumped element lowpass prototype can be implemented merely using capacitors, when inductors are replaced with admittance inverters. In active filters, inverters are implemented using gyrators. However, in order to mitigate the impact of the negative transconductance in the first stage, it is possible to remove the negative feedback in this stage. This results in decoupling of the first stage from the rest of the filter. Therefore, the synthesis of any odd-order all-pole filter (a filter with no finite-frequency transmission zeros such as Butterworth and Chebyshev) is turned into synthesis of a first-order stage cascaded with a even-order filter section, decoupled using a very low output admittance gain block. This means that the even-order filter section needs to be synthesized as a singly-terminated network [21]. Such a network synthesis is shown in Fig. 5.

The transmission transfer function of a two-port lossless all-pole filtering network can be defined as a ratio of two polynomials

$$H(s) = \frac{P(s)}{E(s)} = \frac{a_0}{s^n + b_{(n-1)}s^{(n-1)} + \dots + b_0}. \quad (1)$$

where $P(s)$ is a constant, $E(s)$ is a Hurwitz polynomial (all its roots are located at left-hand side of the complex frequency plane, s -plane), and n is the order of filter.

In all-pole filters, $H(s)$ only has poles, which are the roots of the polynomial $E(s)$. Since the element values of the singly-terminated network in Fig. 5 are real, all coefficients of polynomials in (1) will be real values. This requires that the poles of (1) either locate on the negative real axis in the s -plane or occur in conjugate pairs (i.e. if $s_k = \sigma_k + j\omega_k$ is a pole, then $s_k^* = \sigma_k - j\omega_k$ is also a pole), in the left-hand side of s -plane. For odd-order all-pole filters, there is just one real pole while the rest of poles are conjugate pairs. Therefore,

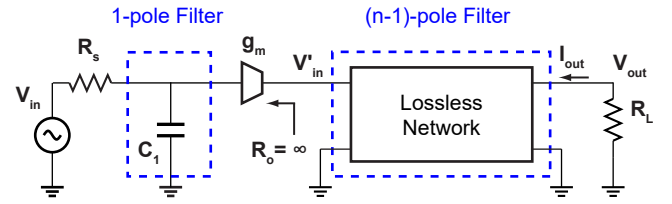


Fig. 5. Decoupling of the first stage in an odd-order all-pole lowpass filter.

if the transfer function of such a filter is expanded using its poles, it can be expressed using (2) at the top of the next page. In this equation, $s_0 = \sigma_0$ is the only real pole with $\sigma_0 < 0$ and s_i ($i = 1, 2, \dots, (n-1)$) are all other poles in the form of conjugate pairs with $\sigma_i < 0$.

This suggests that the transfer function can be decomposed into

$$H_1(s) = \frac{1}{(s - s_0)}, \quad (3a)$$

and

$$\begin{aligned} H_2(s) &= \frac{a_0}{\prod_{k=1}^{(n-1)/2} [s^2 - 2\sigma_k s + (\sigma_k^2 + \omega_k^2)]} \\ &= \frac{a_0}{s^{(n-1)} - 2 \sum_{k=1}^{(n-1)/2} \sigma_k s^{(n-2)} + \dots + \prod_{k=1}^{(n-1)/2} (\sigma_k^2 + \omega_k^2)} \\ &= \frac{a_0}{s^{(n-1)} + b'_{(n-2)} s^{(n-2)} + \dots + b'_0}. \end{aligned} \quad (3b)$$

where $H_1(s)$ is implemented using capacitor C_1 in Fig. 5 with $C_1 = -(1/s_0)$ and $H_2(s)$ is a filter of order $(n-1)$, which needs to be synthesized as a singly-terminated network.

In order to synthesize $H_2(s)$ as a singly-terminated network with $(n-1)$ conjugate pair poles, it should be linked to the driving-point admittance function, $y_{22}(s)$, and trans-admittance function, $y_{12}(s)$, of the network. To this end, as shown in Appendix I, it is required to decompose the denominator of $H_2(s)$ into odd and even polynomials and then divide both the numerator and denominator to the odd portion of the denominator. From this process, $y_{12}(s)$ and $y_{22}(s)$ can be constructed as

$$y_{12}(s) = -\frac{a_0}{b'_{(n-2)} s^{(n-2)} + b'_{(n-4)} s^{(n-4)} + \dots + b'_3 s^3 + b'_1 s}, \quad (4a)$$

and

$$y_{22}(s) = \frac{s^{(n-1)} + b'_{(n-3)} s^{(n-3)} + \dots + b'_2 s^2 + b'_0}{b'_{(n-2)} s^{(n-2)} + b'_{(n-4)} s^{(n-4)} + \dots + b'_3 s^3 + b'_1 s}. \quad (4b)$$

Various methods, such as element extraction, can be used to construct the singly-terminated network by simultaneously realizing $y_{12}(s)$ and $y_{22}(s)$. Therefore, the lossless network in Fig. 5 is implemented as a ladder LC lowpass filter. By finding

$$\begin{aligned}
 H(s) &= \frac{P(s)}{E(s)} = \frac{a_0}{(s - s_0)[(s - s_1)(s - s_1^*)(s - s_2)(s - s_2^*) \dots (s - s_{(n-1)/2})(s - s_{(n-1)/2}^*)]} \\
 &= \frac{a_0}{(s - s_0)[(s^2 - 2\sigma_1 s + (\sigma_1^2 + \omega_1^2)) \cdot (s^2 - 2\sigma_2 s + (\sigma_2^2 + \omega_2^2)) \dots (s^2 - 2\sigma_{(n-1)/2} s + (\sigma_{(n-1)/2}^2 + \omega_{(n-1)/2}^2))]} \\
 &= \frac{a_0}{(s - s_0) \prod_{k=1}^{(n-1)/2} [s^2 - 2\sigma_k s + (\sigma_k^2 + \omega_k^2)]}.
 \end{aligned} \tag{2}$$

the element values of the network, the synthesis is completed. Appendix I shows a recursive method for realizing such a network.

In order to completely realize the filter using only capacitors, the series inductors, L_k , are replaced by shunt capacitors, C_k , and admittance inverters, J_k . The value of admittance inverters (also known as J-inverters), which can be implemented using gyrators, g_{mk} , are found from

$$J_k^2 = g_{mk}^2 = \frac{C_k}{L_k}. \tag{5}$$

Finally, since the coupling matrix of a bandpass filter is the same as ones of its lowpass prototype [22], the decoupled lowpass filter can be readily transformed to a bandpass filter, without changing the coupling values. It is accomplished using converting the shunt capacitors to shunt LC resonators according to

$$L_k = \frac{1}{\omega_o^2 C_k}, \tag{6}$$

where $\omega_o = 2\pi f_0$ is the center frequency of the bandpass filter in rad/sec. Fig. 6 summarizes all the steps required for synthesizing of an all-pole filter with a decoupled first stage.

C. Design Example

In this section, a fifth-order Butterworth lowpass filter is synthesized in the form of a decoupled single-pole stage and a singly-terminated fourth-pole portion, as an example to demonstrate how the above method is used.

In the case of odd-order Butterworth filters, $H_1(s)$ and $H_2(s)$, defined in (3a) and (3b) respectively, are simplified to

$$H_1(s) = \frac{1}{(s + 1)}, \tag{7a}$$

and

$$H_2(s) = \frac{1}{\prod_{k=1}^{(n-1)/2} [s^2 + 2 \sin(\theta_k) s + 1]}, \tag{7b}$$

where θ_k is the angle between two consequence poles [23] and is calculated using

$$\theta_k = (2k - 1) \frac{\pi}{2n} \quad k = 1, 2, \dots, n. \tag{8}$$

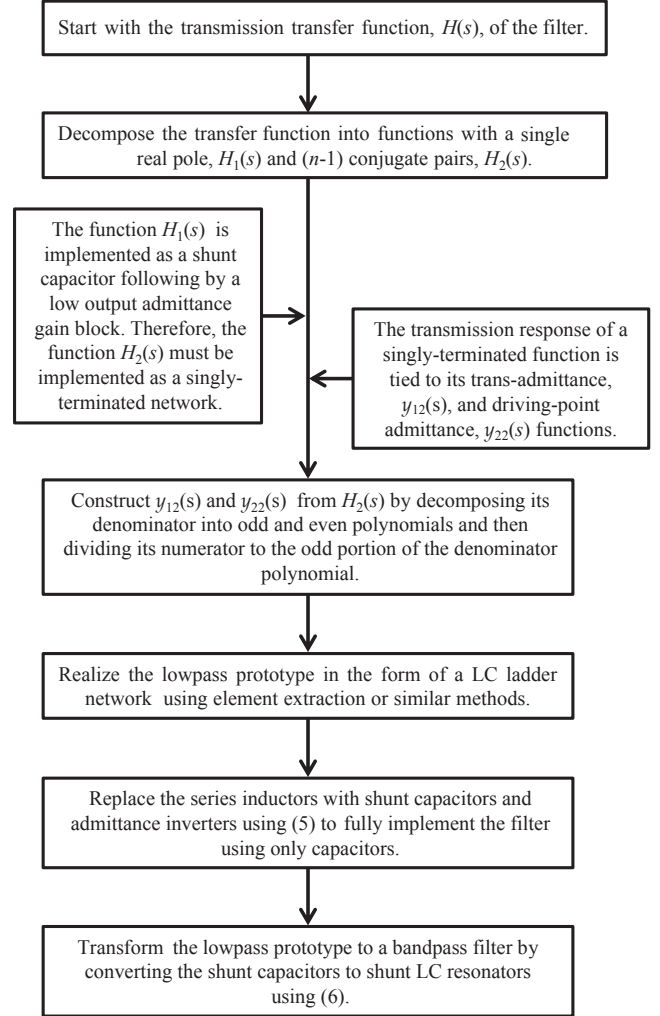


Fig. 6. Required steps for synthesis of a filter with a decoupled first stage.

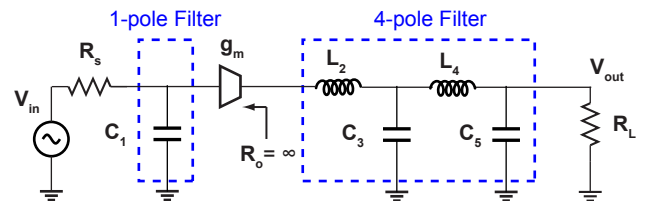


Fig. 7. 5th-order Butterworth lowpass filter with a decoupled first stage.

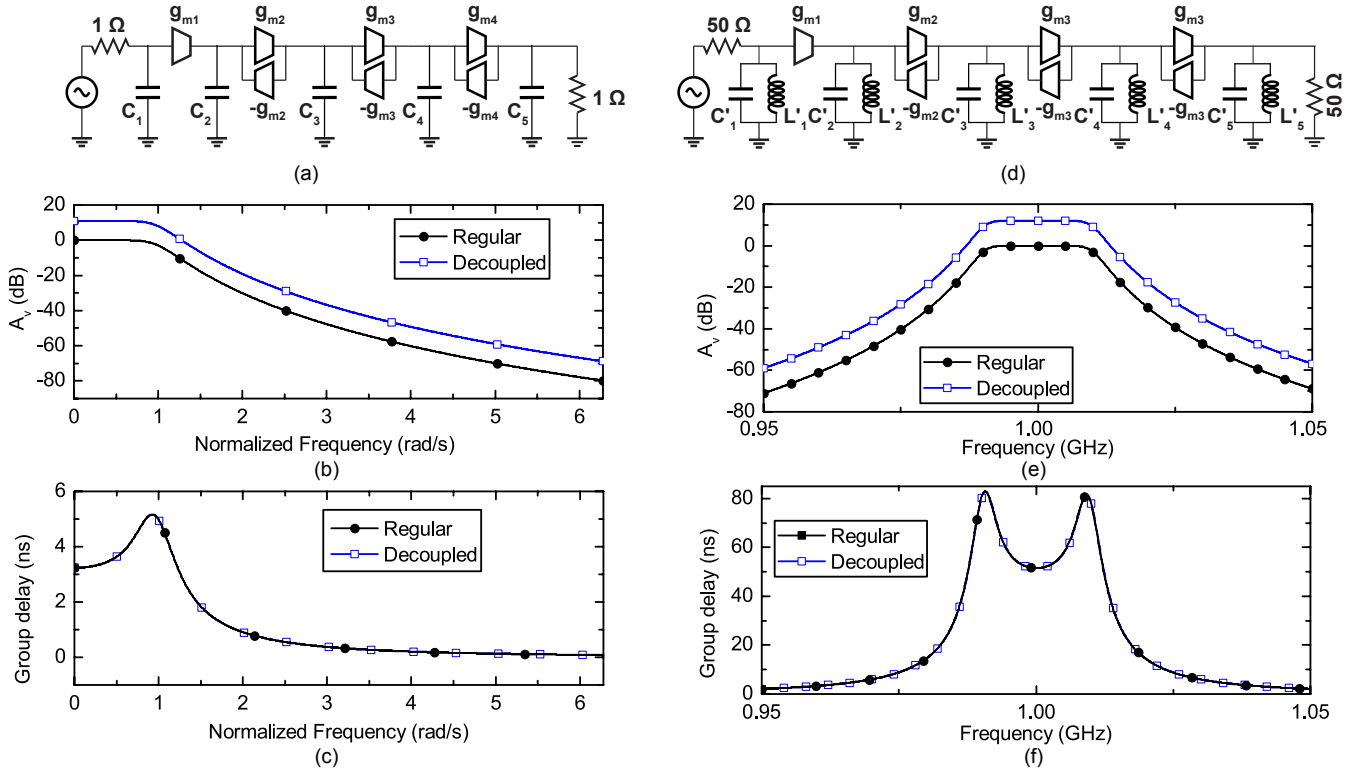


Fig. 8. Schematics and responses of properly synthesized decoupled LPF and BPF. (a) First stage decoupled normalized LPF for a fifth-order Butterworth filter. (b) Magnitude response and (c) group delay with and without decoupling the first stage. (d) First stage decoupled normalized BPF for a fifth-order Butterworth with $f_0 = 1$ GHz and $BW = 20$ MHz. (e) Magnitude response and (f) group delay with and without decoupling the first stage.

Therefore, for a fifth-order Butterworth filter, $H_2(s)$ will be

$$\begin{aligned} H_2(s) &= \frac{1}{(s^2 + 0.6180s + 1) \cdot (s^2 + 1.6180s + 1)} \\ &= \frac{1}{s^4 + 2.2360s^3 + 3s^2 + 2.2360s + 1}. \end{aligned} \quad (9)$$

Applying the synthesis technique described in the previous section to (9) yields

$$y_{12}(s) = -\frac{1}{2.2360s^3 + 2.2360s} \quad (10a)$$

and

$$y_{22}(s) = \frac{s^4 + 3s^2 + 1}{2.2360s^3 + 2.2360s}. \quad (10b)$$

Following the process shown in Appendix I, the element values for constructing the singly-terminated network $H_2(s)$ are found. Table I lists the element values for a regular and the decoupled fifth-order Butterworth lowpass filter. Note that from (7a), the capacitor value in the first decoupled stage is $C_1 = 1.0$ F. Therefore, the circuit is fully synthesized. Such a decoupled-first-stage, fifth-order Butterworth filter is shown in Fig. 7.

Using (5), the inductors in Fig. 7 can be substituted by capacitors and gyrators. The schematic of the decoupled fifth-order Butterworth lowpass filter, fully implemented by shunt capacitors, is depicted in Fig. 8(a). Table I gives the element values for the filter fully implemented by shunt capacitors. Fig. 8(b) shows a comparison of the magnitude of the transfer function for the regular and decoupled structure. The exact

TABLE I
ELEMENT VALUES FOR THE FIFTH ORDER BUTTERWORTH LPF

Lowpass Prototype	Decoupled Structure	Implementation
C_1	C_1	C_1
L_2	L_2	C_2
C_3	C_3	C_3
L_4	L_4	C_4
C_5	C_5	C_5

match between the two validates the synthesis procedure. The decoupled filter provides extra gain due to decoupling of the first stage while maintaining the passband shape and bandwidth (BW) constant. The group delay for these two scenarios is also identical as shown in Fig. 8(c) due to exact filter synthesis. The choice of g_{m2} and C_2 depends on the designer. The gain of the filter increases as well as the NF reduces by lowering the negative g_m cells. However, the linearity degrades with lower g_m values. Finally, Fig. 8(d) shows the corresponding decoupled fifth-order Butterworth bandpass filter after impedance scaling and frequency transformation with $R_s = R_L = 50$ Ohm, $f_0 = 1$ GHz and $BW = 20$ MHz [24]. Figs. 8(e) and (f) also depict the magnitude response and group delay of the decoupled bandpass filter compared to those of the regular implementation, respectively. It is observed that similar to the lowpass filter, not only an extra gain is added to the filter, the passband shape and bandwidth of the filter is maintained. This is while the group delay is kept the same.

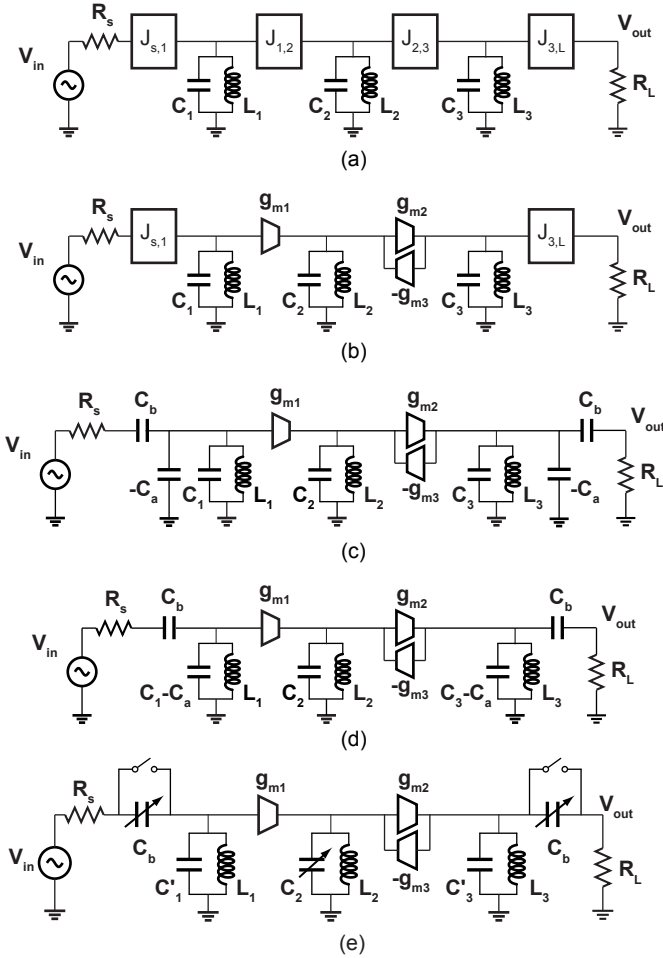


Fig. 9. Reconfiguring a Butterworth filter to a Chebyshev filter with variable bandwidth. (a) A Butterworth filter can be transformed to a similar bandwidth Chebyshev filter using gyrators/J-inverters. (b) Decoupling the first stage. (c) Implementation of source and load J-inverters. (d) The negative capacitance is absorbed in C_1 and C_3 . (e) Component tunability to obtain desired filter response.

III. TUNABLE FILTER BANDWIDTH AND SHAPE

It is often desirable to reconfigure the filter shape and bandwidth as well as the center frequency of the filter to cope with the dynamic environment [25]–[27].

In coupled-resonator filters, such as the one shown in Fig. 9(a), the filter bandwidth is predominantly determined by the inter-resonator couplings if identical resonators are used. In the proposed N-path filter design, the inter-resonator coupling is realized by active gyrators (J-inverter) consisting of back-to-back connected transconductance amplifiers (Fig. 9(b)). The inverter value can be changed by changing the g_m value of the gyrator. However, this approach results in significant trade-off between the bandwidth and the power consumption of the filter; more power is needed for larger bandwidth. To resolve this issue, it is opted to tune resonators in this work. In terms of N-path filter implementation, this means tuning the baseband capacitors $C_{B,x}$ in Fig. 2(c).

In addition to tuning the internal couplings, the external couplings also need to be adjusted to transform the filter shape or bandwidth with proper matching, while maintaining the C_1

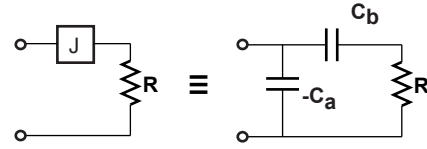


Fig. 10. A possible way for implementation of J-inverters in integrated circuits.

TABLE II
ELEMENT VALUES FOR A THIRD ORDER BUTTERWORTH LPF WITH
40 MHz BANDWIDTH

Lowpass Prototype		Denormalized LPF		Decoupled First Stage	
C_1	1	C_1	79.57 pF	C_1	79.57 pF
L_2	2	L_2	397.88 nF	C_2	9.94 pF
C_3	1	C_3	79.57 pF	C_3	79.57 pF

& C_3 constant. This can be achieved by placing inverters at the ports (that is $J_{S,1}$ and $J_{3,L}$ in Fig. 9(a)). These inverters are essentially impedance transformers and are used to scale the source and load impedances to arbitrary values. They can also be realized by a stacked capacitor transformer for easy on-chip integration as shown in Fig. 10. Fig. 9(c) shows how the external couplings in the coupled-resonator filter are replaced with the stacked capacitor transformer. The values of the capacitors can be readily calculated from

$$C_b = \frac{J}{\omega_o \sqrt{(1 - (JR)^2)}} \quad (11a)$$

and

$$C_a = \frac{-J\sqrt{(1 - (JR)^2)}}{\omega_o}, \quad (11b)$$

where J is either $J_{S,1}$ or $J_{3,L}$ as in Fig. 9(a). The negative C_a can be absorbed in C_1 or C_3 as shown in Fig. 9(d). In practice, C_a is much smaller than both C_1 and C_3 . To implement a tunable bandwidth, C_b and C_2 need to be adjusted.

To understand the range of values for the tuning components, a design example is given here for a third order filter with a variable bandwidth from 20 MHz to 40 MHz, whose shape can be reconfigured between a Butterworth response and a Chebyshev one with arbitrary ripple levels. The nominal values of the components for a Butterworth lowpass filter configuration with 40 MHz bandwidth is listed in Table II. C_2 is calculated from (32b) for $g_{m2} = 10$ mS, $g_{m3} = 5$ mS and corresponding L_2 . The LPF can then be transformed into a BPF using (6). The schematic of the filter follows Fig. 9(e).

The coupling capacitor C_b is varied based on the frequency and bandwidth requirements. Fig. 11 shows the calculated required component values for a Butterworth configuration with various bandwidth. The coupling capacitor C_b is calculated at 0.2 GHz and 1 GHz to cover the whole tuning range. As the frequency changes from 0.2 GHz to 1 GHz, C_b needs to be changed from 3.18 pF to 42.1 pF. The nominal values of the capacitors are chosen based on the Butterworth configuration with 40 MHz bandwidth. Therefore, C_b is not required for that

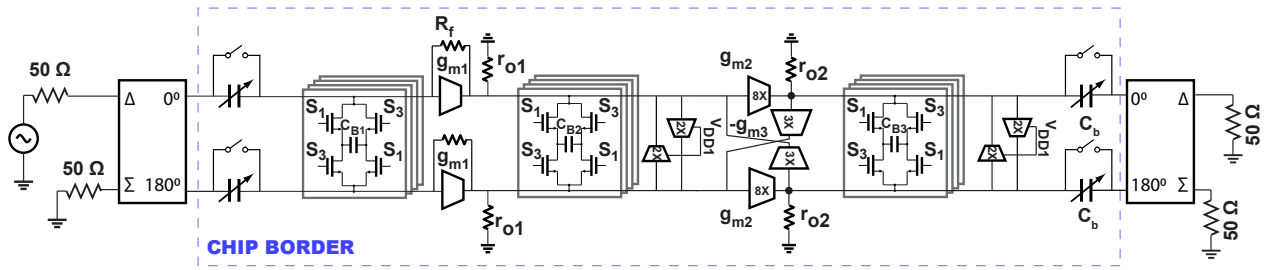
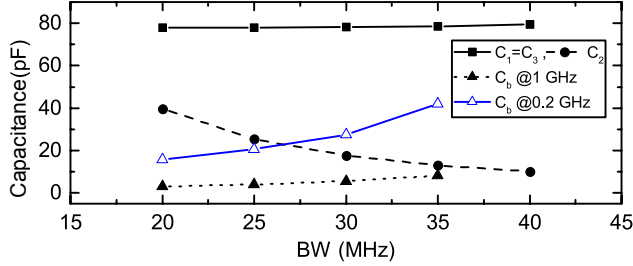
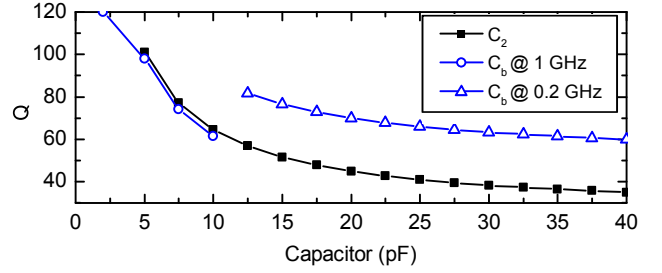
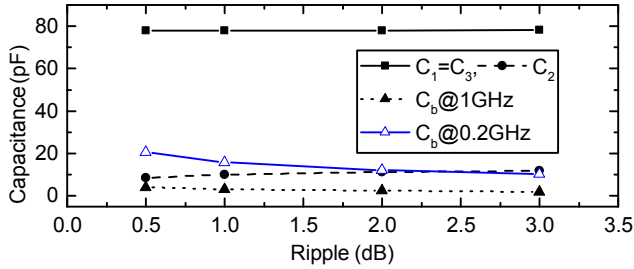


Fig. 13. Full implementation of the proposed filter.


 Fig. 11. Component values of the proposed filter as Butterworth configuration with different bandwidth. C_b is calculated at $f_0 = 0.2$ GHz and 1 GHz.

 Fig. 14. Quality factor for the tuning capacitors C_2 at 1 GHz and C_b at 0.2 GHz and 1 GHz.

 Fig. 12. Component values of the proposed filter as Chebyshev configuration with different ripple level. C_b is calculated at $f_0 = 0.2$ GHz and 1 GHz.

configuration (no point for C_b in Fig.11 for $BW = 40$ MHz) or in other words, C_b is shorted with the top switch in Fig. 9(e). As a result, the filter looks similar as Fig. 8(d) for this specific configuration.

In a similar fashion, by adjusting $C_1(=C_3)$, C_2 , C_a , and C_b , it is possible to reconfigure the filter into a Chebyshev response with different ripple levels. Fig. 12 shows the required component values for the Chebyshev configuration with 40 MHz bandwidth and different ripple level.

The parallel LC tanks can be realized with N-path filters, where the center frequency is determined by the clock frequency. The corresponding baseband capacitors $C_{B1}(=C_{B3})$ and C_{B2} in Fig. 2(c) can be calculated from [12]

$$C_{Bx} = C_x \frac{m [N \sin^2(\pi D) + D\pi^2(1 - ND)]}{ND\pi^2}, \quad (12)$$

where $m = 2$ for the single-ended circuit and $m = 8$ for the differential network. In a lumped prototype, the absorption of C_a into C_1 has two effects. It changes both the center frequency and the bandwidth of the resonators. However, on

the other side, in a N-path implementation the absorption of the negative capacitance only changes the bandwidth of the resonator as the center frequency is determined primarily by the clock frequency. Therefore, there can be a slight difference between the lumped prototype and the actual implementation in terms of filter BW. However, the filter BW can be adjusted by tuning either C_b or C_2 .

IV. FILTER IMPLEMENTATION

The full implementation of the proposed filter is shown in Fig. 13. Large NMOS RF switches of $W/L = 80 \mu\text{m}/60 \text{nm}$ (on-resistance of approximately 4.2Ω) are used to reduce the noise, non-linearity and mismatch between them. The switches are driven by 25% duty cycle 4-phase non-overlapping clocks. A differential structure is exploited for the proposed architecture to suppress common-mode disturbance as well as the differential baseband capacitors reduce the total area. MIM capacitor with underlying metal are used for the baseband capacitors. The resistors are realized with N+ poly resistor without silicide. Each switch is biased at 900-mV DC voltage (VCLK) to provide full 1.2-V swing to maximize the linearity of the switches. Instead of using a single varactor, a switched-bank of capacitor is used to implement C_b for maintaining a reasonable Q. Fig. 14 shows the Q for the tuning capacitors C_2 at 1 GHz and C_b at 0.2 GHz and 1 GHz. The simulated Q of the switched capacitor bank ranges from 40 to 100. Within this Q range, the insertion loss degradation is less than 1 dB. This insertion loss variation can be compensated by gain adjustments through the g_m cells. The negative g_{m3} in Fig. 9(e) can be easily implemented by flipping the connection in a differential configuration.

The switch size used along with C_b is $120 \mu\text{m}/60 \text{nm}$, with an on-resistance of 3.6Ω and C_{off} of 42.3 fF. The choice of

TABLE III
FILTER PERFORMANCE BASED ON DIFFERENT PARAMETERS

Parameter	Gain	NF	IIP3	BW	Power
$g_{m1} \uparrow$	\uparrow	\downarrow	\downarrow	-	\uparrow
$g_{m2} \uparrow$	-	\downarrow	\uparrow	\uparrow	\uparrow
$g_{m3} \uparrow$	\downarrow	\uparrow	\uparrow	\uparrow	\uparrow

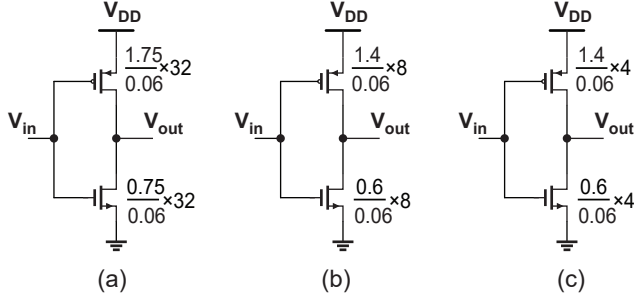


Fig. 15. Configuration of g_m cells. (a) g_{m1} , (b) g_{m2} , and (c) g_{m3} .

g_{m1} depends on the gain requirements as the overall filter gain can be approximated as $A_v = (g_{m1}/g_{m3})\text{sinc}^2(\pi/4)$. The value of C_2 depends on L_2 , g_{m2} , and g_{m3} according to (5). To achieve higher stopband rejection, g_{m2} and g_{m3} need to be reduced, however g_{m2} need to be increased and g_{m3} need to be reduced from noise point of view [5]. The impact of different parameters on the filter performance is listed in Table. III. In the prototype design the g_m values are, $g_{m1} = 48.17$ mS, $g_{m2} = 10$ mS and $g_{m3} = 5$ mS. The g_m cells are shown in Fig. 15. The output impedance of g_{m1} , g_{m2} and g_{m3} are 124.45 Ω , 592.7 Ω and 1.18 k Ω , respectively.

A master clock (CLK) at 4 times the switching frequency is applied from off-chip. A D-flip-flop (D-FF) based divider divides the input clock by 4 while an AND gate generates the required 25% duty cycle clock [28]. A shift register implemented with transmission gate flip-flops produces 4-phase clocks to drive the switches.

A. Non-Ideal Effects Mitigation

The finite on-resistance R_{sw} of the switches reduces the Q of the baseband capacitors. It modifies the pole of the filter and introduces extra zeros in the transfer function, which is responsible for limited stopband rejection of the overall filter [8]. As an example, the effect of finite switch resistance ($R_{sw} = 5 \Omega$) on Butterworth and 0.5 dB ripple Chebyshev filter is shown in Fig. 16. The out-of-band rejection degrades with higher switch resistance. The resistance of the switch parallel with the coupling capacitor C_b also lowers the Q of the filter. A large switch size is chosen to mitigate this effect. However, the parasitic capacitance associated with the switch shifts the center frequency as well as increase the insertion loss.

In addition, the non-zero switch resistance reduces the Q of baseband capacitors, which reduces the Q of the overall filter. As a result, it is necessary to model the corresponding parasitic resistance for the lumped prototype due to the switch resistance and the output impedance of the transconductor cell.

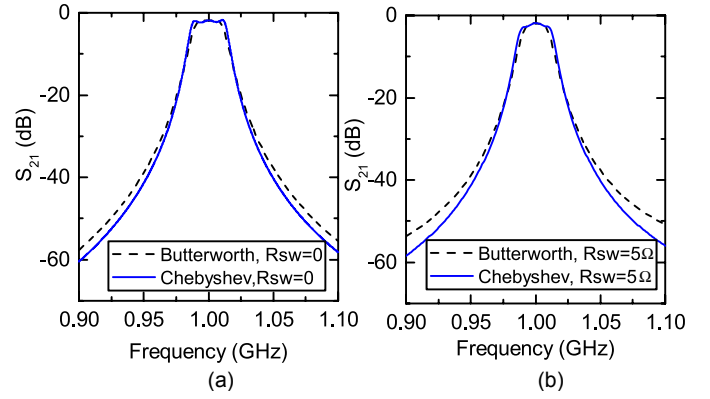


Fig. 16. Simulated comparison of Butterworth and Chebyshev type N-path filters with (a) $R_{sw} = 0$ and (b) $R_{sw} = 5 \Omega$.

A 3-pole N-path filter and its corresponding lumped model is shown in Fig. 17. Following the procedure shown in [5], the equivalent output impedance for different N-path sections can be found as shown in Fig. 17(a)

$$R_{p1} = \frac{N [1 - \cos(2\pi D)] R_s + 2D\pi^2 (R_s(1 - ND) + 2R_{sw})}{2N(D\pi)^2 - N(1 - \cos(2\pi D))}, \quad (13)$$

$$R_{p2} = \frac{N [1 - \cos(2\pi D)] R_{o1} + 2D\pi^2 [R_{o1}(1 - ND) + 2R_{sw}]}{2N(D\pi)^2 - N [1 - \cos(2\pi D)]}, \quad (14)$$

$$R_{p3} = \frac{N [1 - \cos(2\pi D)] R_{o2} + 2D\pi^2 [R_{o2}(1 - ND) + 2R_{sw}]}{2N(D\pi)^2 - N [1 - \cos(2\pi D)]}, \quad (15)$$

where R_{o1} and R_{o2} are the impedances seen after g_{m1} and g_{m2} . The output impedance of g_{m1} , g_{m2} and g_{m3} are 124.45 Ω , 592.7 Ω and 1.18 k Ω , respectively. R_{P1} , R_{P2} and R_{P3} is calculated as 266.7 Ω , 585.3 Ω and 750 Ω , respectively for $R_{sw} = 5 \Omega$.

The finite output impedance of the g_m cells are shown in Fig. 17(b). The finite output impedance of the g_m cells load the resonant tanks and also reduce the Q of the filter. In the prototype implementation, negative resistances are added after the g_m cells as shown in Fig. 17(b) to compensate for the losses from the output impedance of g_m cells as well as the switch losses. However, the large amount of negative admittance reduces the filter dynamic range as well as increases the power consumption. These negative resistors are made with back-to-back inverters. The back-to-back inverters have a separate supply voltage with a nominal value of 1.2 V. The negative resistance increases the overall noise of the filter. The noise factor due to negative resistors are $g_{m,neg1}/(g_{m1}^2 A_1^2 R_s)$ and $g_{m,neg2}/(g_{m1}^2 g_{m2}^2 r_{o1}^2 A_1^2 R_s)$ as described in [5], [8], where $g_{m,neg1,2}$ are the G_m cells added to the internal nodes of the filter to control $r_{o1,2}$, $A_1 = \text{sinc}(\pi/4)$ and R_s is the source resistance.

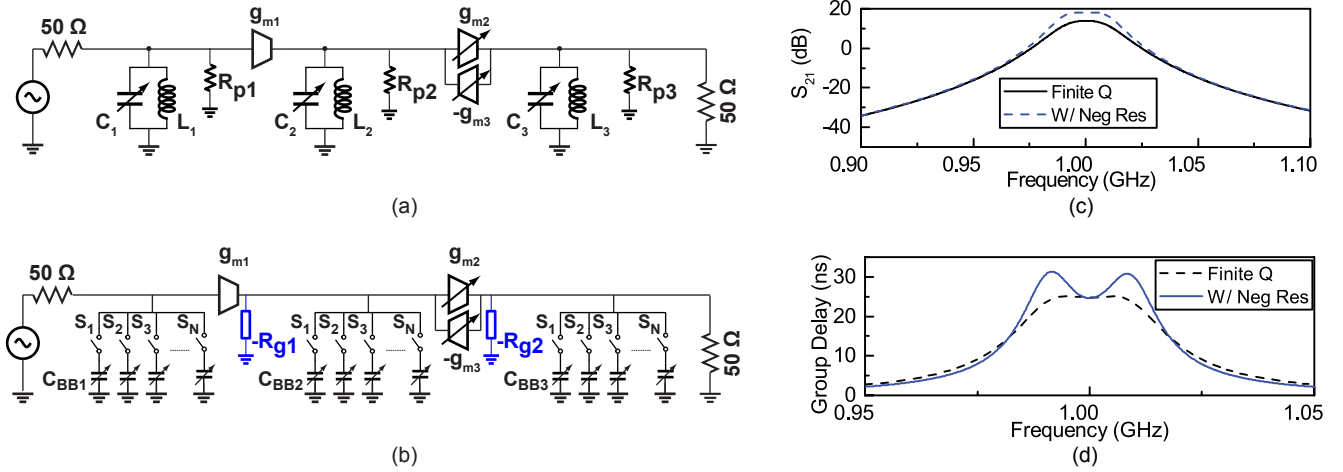


Fig. 17. Effect of finite output impedance of g_m cell and the utilized solution. (a) Lumped model of a 3-pole N-path filter with finite output impedance of the g_m cells loading the tanks. (b) Negative resistances are added to compensate for the loading. (c) S_{21} for both cases. (d) Group delay for both cases.

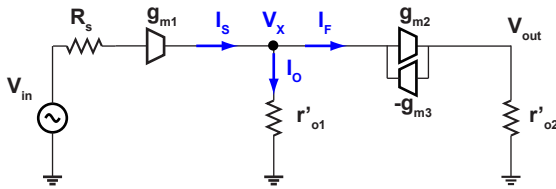


Fig. 18. Simplified model used to calculate the IIP3 of the filter.

B. Linearity Analysis

It is highly desirable for a front-end filter to be extremely linear to tackle strong out-of-band blockers. In an long-term-evolution (LTE) receiver, for example, transmit leakage introduces a out-of-band (OOB) blocker at different frequency offset to primary and diversity receivers which places stringent linearity and power handling capability requirement for the front-end filter. In this section, the linearity of the proposed filter is derived using the simple equivalent model shown in Fig. 18.

Writing equations at the V_{out} node, by considering the first and the third non-linear terms, yields

$$g_{m2,1}V_x + g_{m2,3}V_x^3 + g_{o2}V_{out} + g_{o2}V_{out}^3 = 0 \quad (16)$$

where $g_{m_{x,1}}$ and $g_{m_{x,3}}$ are the transconductance of g_m cells associated with the first and third harmonics. r'_{o1} is the combined resistance of r_{o1} , R_{P2} and $-R_{g1}$. Similarly, r'_{o2} is the combined resistance of r_{o2} , R_{P3} , R_L and $-R_{g2}$.

The feedback current at the gate of g_{m2} can also be expressed as

$$I_F = -g_{m3,1}V_{out} - g_{m3,3}V_{out}^3. \quad (17)$$

The output current of g_{m1} is

$$I_s = -g_{m1,1}V_{in} - g_{m1,3}V_{in}^3. \quad (18)$$

It is possible to represent the output voltage V_{out} as (see Appendix)

$$V_{out} = \alpha_1 V_{in} + \alpha_3 V_{in}^3, \quad (19)$$

where

$$\alpha_1 = \frac{g_{m1,1}}{g_{m3,1} + \frac{1}{g_{m2,1}r'_{o1}r'_{o2}}}, \quad (20)$$

and

$$\alpha_3 = \frac{g_{m1,3}}{g_{m3,1} + \frac{1}{g_{m2,1}r'_{o1}r'_{o2}}} - \left(\frac{g_{m1,1}}{g_{m3,1} + \frac{1}{g_{m2,1}r'_{o1}r'_{o2}}} \right)^3 \times \frac{A - g_{m2,3}r'_{o2}}{g_{m2,1}^4 r'_{o1} r'_{o2} \left(\frac{1}{g_{m2,1}r'_{o1}r'_{o2}} + g_{m3,1} \right)},$$

where $A = g_{m2,1}^4 g_{m3,3} r'_{o1} r'_{o2} - g_{m2,1}^3 r'_{o2}^3$.

Assuming $g_{m3,1} \gg \frac{1}{g_{m2,1}r'_{o1}r'_{o2}}$,

$V_{out} =$

$$\frac{g_{m1,1}}{g_{m3,1}}V_{in} + \left(\frac{g_{m1,3}}{g_{m3,3}} + \frac{g_{m1,1}^3}{g_{m3,1}^3} \times \frac{A - g_{m2,3}r'_{o2}}{g_{m2,1}^4 g_{m3,1} r'_{o1} r'_{o2}} \right) V_{in}^3 \quad (21)$$

The in-band input referred third order intercept point (IIP3) calculated based on (21) with variations in g_{m2} and g_{m3} is shown in Fig. 19 (a). The IIP3 increases with increase in both g_{m2} and g_{m3} . Fig. 19 (b) shows the simulated bandwidth of the filter with g_{m2} and g_{m3} . The bandwidth also increases with higher g_{m2} , g_{m3} . However, by increasing g_{m2} and g_{m3} , power consumption increases and the gain of the filter drops. In terms of noise, it is required to increase g_{m2} and reduce g_{m3} [14].

V. MEASUREMENT RESULTS

The filter is fabricated in a 65-nm CMOS technology. The chip has an area of 1.1 mm² including the bond pads (Fig. 20). The circuit is wire-bonded and tested on a printed circuit board. An off-chip balun (MACOM MABA-010247-2R1250) is used to transform a single-ended signal to a differential signal. The typical insertion loss of the balun is approximately 1 dB.

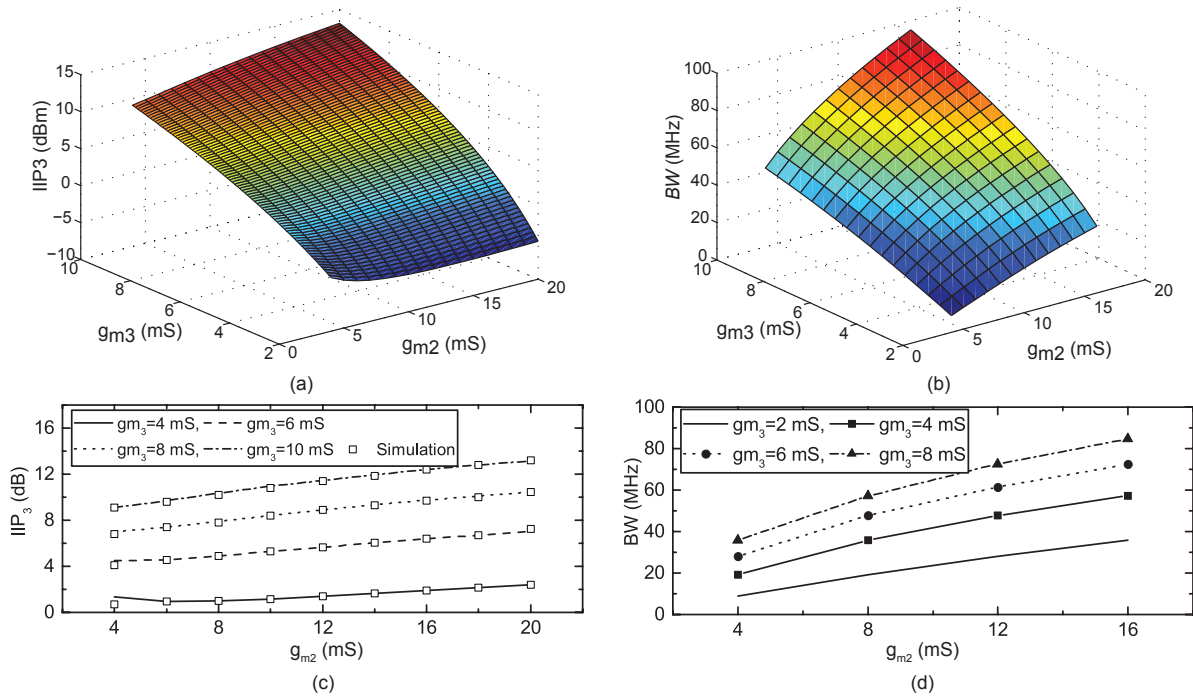


Fig. 19. Variation of the in-band IIP3 and bandwidth of the filter versus g_{m2} and g_{m3} . (a) Theoretical in-band IIP3 of the filter with g_{m2} and g_{m3} variations from (21). (b) Simulated bandwidth of the filter with g_{m2} and g_{m3} variations. (c) Analytical and simulated IIP3 of the filter shown for some specific values of g_{m2} and g_{m3} . (d) Bandwidth of the filter shown for some specific values of g_{m2} and g_{m3} from (b).

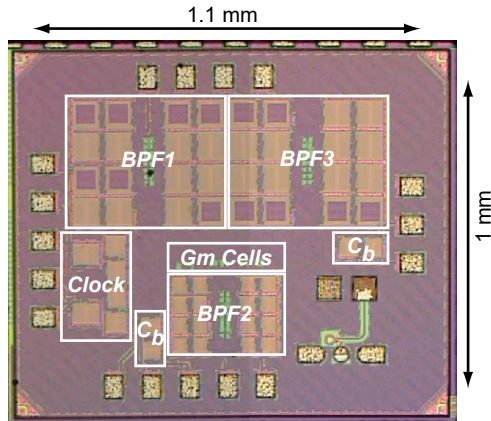


Fig. 20. Chip micrograph of the proposed filter. The total chip area is 1.1mm^2

A. Frequency Response

Fig. 21 compares the measured and simulated filter response for Butterworth configuration with target BW of 20 MHz. The responses are in good agreement and very minor discrepancies are observed. The center frequency of the measured response is 1 MHz lower than the simulated response due to extra layout parasitics. The out-of-band rejection is 3 dB lower due to slightly higher R_{sw} and extra parasitic coupling capacitors.

Fig. 22(a, b, & c) show the measured S_{21} , S_{11} and zoomed-in view of S_{21} , over the entire tuning range of 0.2–1.2 GHz for a Butterworth passband configuration. The S_{11} shows good match between 0.4 GHz and 1 GHz, but degrades toward 0.2 GHz and 1.2 GHz. This degradation is primarily due to the limited bandwidth of the input balun. There are multiple

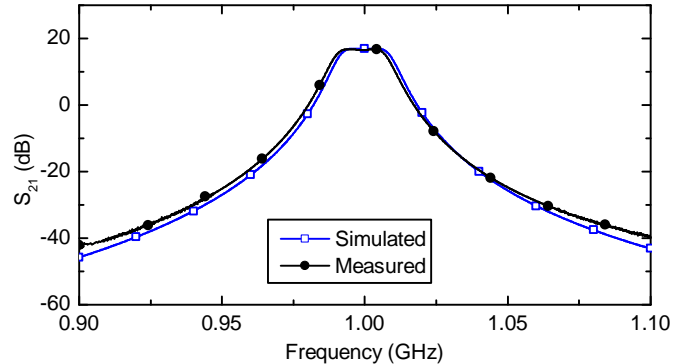


Fig. 21. Comparison of the measured filter response with the simulated response for Butterworth configuration with a target BW of 20 MHz.

ways to improve the matching. However, there are trade-offs associated with matching, NF and gain. As an example, reducing R_f in Fig. 13 improves S_{11} while it degrades the NF. The zoomed-in view of S_{21} shows the BW as well as the passband ripple, which is lower than 0.25 dB for all cases. The filter shows a gain of 14.5–16 dB, and 3-dB bandwidth of 18.8–20.2 MHz. The parasitic capacitance at each node of the filter modifies the equivalent resistance of that node, which degrades the effective unloaded Q. As a result, the gain of the filter decreases at higher frequencies. The parasitic capacitance also lowers the center frequency of the switched-capacitor sections and the detailed analysis was shown in [5], [8]. However, as the center frequency of the filter is tunable, this is not a concern. The filter draws 18.7 mA, and the LO chain draws 3.2 mA to 15.87 mA from 1.2 V in the whole

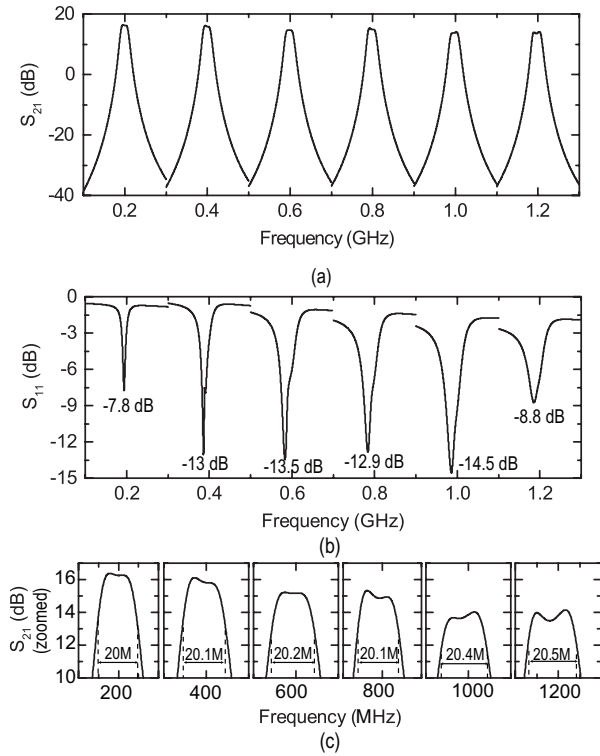


Fig. 22. Measured response of the proposed filter configured as Butterworth type over the whole tuning range for a target bandwidth of 20 MHz, (a) S_{21} at uniformly-spaced center frequencies, (b) corresponding S_{11} with the maximum depths labelled, and (c) zoomed-in view of the passband response to clearly show the BW. Each window corresponds to a frequency span of 40 MHz.

tuning range. The clock buffer power consumption is 13.4 mW. The LO feedthrough to the input port of the filter is -65 dBm at a center frequency of 1 GHz.

The proposed filter can be reconfigured in Butterworth, Chebyshev-0.5 dB ripple and Chebyshev-3 dB ripple with proper tuning of C_b and C_2 . For example, the tunability of the proposed filter for 0.5-dB ripple Chebyshev configuration is shown in Fig. 23(a) for 20-MHz bandwidth. Fig. 23(b) shows the close-in response at 1 GHz with different ripple levels. It is possible to increase the stopband rejection of the filter with higher passband ripple.

The filter can also be reconfigured in terms of bandwidth. For example, Fig. 24 shows the filter response for both Butterworth and Chebyshev-3 dB ripple configuration with target bandwidth of 40 MHz. The filter has more loss at higher frequencies due to g_m cells. The primary objective of the proposed filter is to reconfigure it smartly based on spectrum requirements.

B. Noise Figure

The measured NF of the filter over the tuning range is shown in Fig. 25(a) for two different bandwidths. The filter has a measured small signal NF of 3.7–5.5 dB over the tuning range of 0.2–1.2 GHz for $BW = 40$ MHz. The NF increases as the bandwidth decreases due to the finite Q and switch loss of C_b . The NF is higher at high frequencies as the gain of the filter decreases.

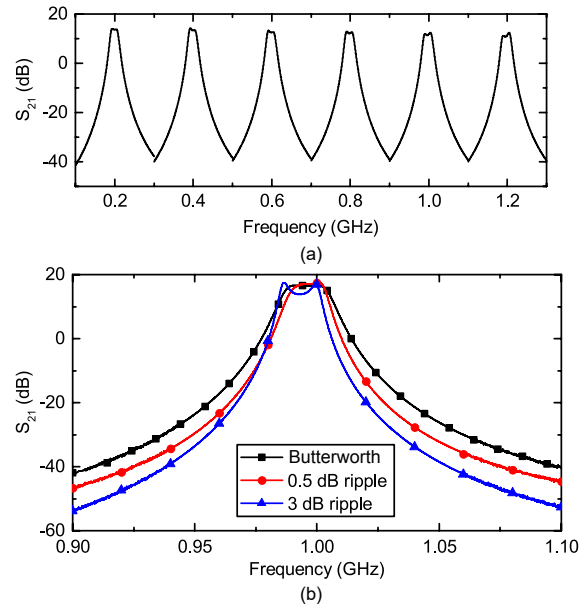


Fig. 23. Measured S_{21} of the prototype filter. (a) Configured as Chebyshev type with 0.5 dB passband ripple for a target bandwidth of 20 MHz, tuned across the tuning range. (b) Close-in response of the filter for three different configurations (Butterworth, 0.5 dB-Chebyshev, and 3 dB-Chebyshev) at 1 GHz.

Measured NF with various blocker power level is shown in Fig. 25(b) with $f_0 = 1$ GHz. In this test, the blocker is placed at 50 MHz offset. The NF increases with increasing blocker power due to reciprocal mixing of the blocker and the LO phase noise. The external LO signals (Keysight E8663D) have an SSB phase noise of -143 dBc/Hz at 100 KHz offset. The simulated phase-noise of on-chip 4-phase LO signals (S_1 , S_2 , S_3 and S_4) with frequency of 1 GHz from the noisy external signal generator is around -150 dBc/Hz at 100 KHz offset. When the blocker mixes with LO phase noise, it deposits additional noise in the receive channel proportional to the blocker amplitude. The proposed filter can tolerate an 10-dBm blocker with $NF < 10$ dB.

C. Group Delay

The measured group delay (GD) of the filter is shown in Fig. 26. The group delay for the Butterworth configuration with different bandwidths is shown in Fig. 26(a) as the GD is inversely proportional to the filter bandwidth. Fig. 26(b) shows the GD for different filter configuration and $BW = 20$ MHz. The GD of the filter over the whole tuning range is shown in Fig. 26(c), where the filter is configured for Butterworth type and $BW = 20$ MHz. This highlights the efficacy of the filter in controlling signal delay characteristics. The GD will be reduced for higher bandwidth.

D. Linearity

To evaluate the linearity of the filter, two-tone IIP3 and compression measurements were carried out and results are shown in Fig. 27(a&b). With the filter tuned to 1 GHz, the two tones are placed at 1.008 GHz and 1.01 GHz for the in-band

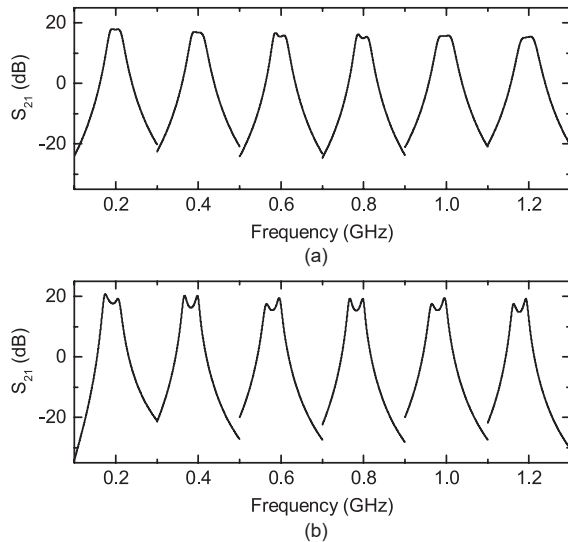


Fig. 24. The measured tunability of the prototype filter configured as Chebyshev type with (a) 0.5 dB passband ripple with a target bandwidth of 40 MHz and (b) 3 dB passband ripple configuration with similar bandwidth.

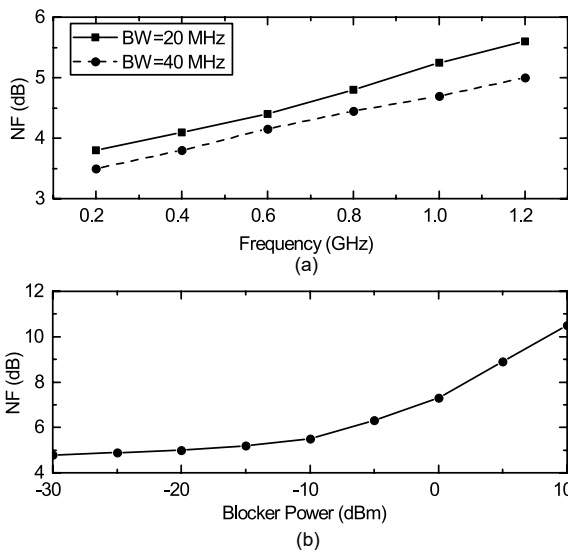


Fig. 25. Measured NF of the filter in Butterworth configuration versus (a) the frequency tuning range and (b) the blocker power.

IIP3 measurement, and 1.05 GHz and 1.09 GHz for the out-of-band IIP3 measurement. The blocker 1-dB compression point (B1dB) is measured by placing an interfering signal at an offset frequency (~ 50 MHz) and observing the compression behavior of the in-band signal while increasing the power of the interferer. B1dB is approximately 8.5 dBm over the tuning range. Out-of-band and in-band IIP3 measured at 1 GHz center frequency are shown in Fig. 27(b).

Finally, a comparison between the performance of the presented filter and other designs reported in literature, is shown in Table. IV. The proposed filter demonstrates the filter shape and center frequency reconfigurability to cope with the dynamic environment. The bandwidth is also tunable while

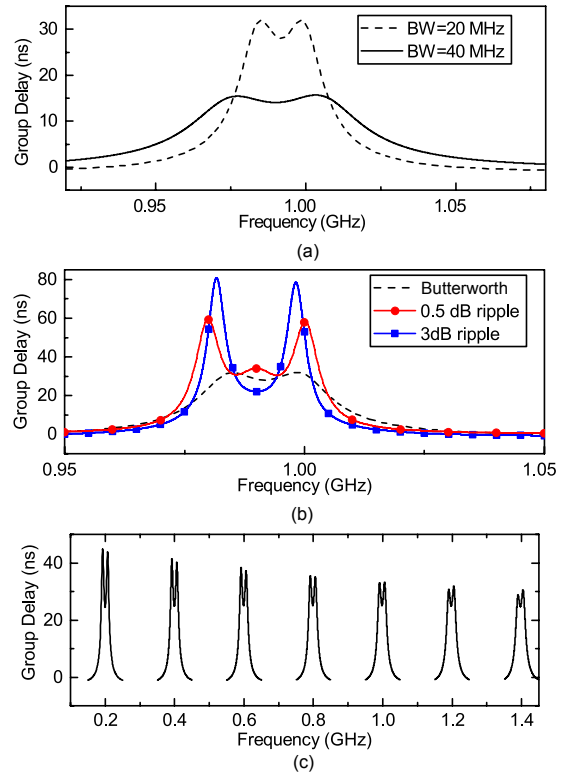


Fig. 26. The measured group delay of the filter for (a) Butterworth configuration with $BW = 20$ MHz and $BW = 40$ MHz, (b) three different configurations (Butterworth, 0.5 dB-Chebyshev, and 3 dB-Chebyshev) all with $BW = 20$ MHz, and (c) Butterworth configuration with $BW = 20$ MHz over the whole tuning range.

the out-of-band linearity is comparable with other state-of-the-art papers. It is also observed that the presented filter provides high gain with lower power consumption.

VI. CONCLUSION

A general analytical synthesis procedure for design and implementation of bandpass filters with N-path architecture is introduced in this paper. Based on the proposed methodology, a third order reconfigurable and tunable N-path bandpass filter is presented. The proposed filter has been implemented in 65nm CMOS technology and can be integrated into the RF transceiver chips. The proposed reconfigurable filter can adjust the rejection level based on the spectrum allocation and channel requirements suitable for software defined radios. The bandwidth of the proposed filter is also tunable to pick up multiple desired frequency bands in a intra-band continuous carrier aggregation scenarios. This filter will enable the implementation of reconfigurable multiband radio with variable bandwidth such as required for LTE.

APPENDIX I GENERAL SYNTHESIS METHOD

The most suitable transfer function describing the singly-terminated network, shown in Fig. 5, are Transfer Admittance ($-Y_{12}$) and Voltage Gain (G_{12}), which can be

TABLE IV
 PERFORMANCE COMPARISON.

	Chen [2]	Darvishi [8]	Amin [29]	Reiskarimian [7]	Xu [3]	Luo [30]	This work
Circuit Type	Receiver	Filter	Filter	Filter	Receiver	LNA	Filter
CMOS Tech (nm)	65 (LP)	65	130 (BiCMOS)	65	65	32 (SOI)	65
Frequency (GHz)	0.5–3	0.1–1.2	4.1–7.9	0.6–0.85	0.3–1.7	0.4–6	0.2–1.2
Gain (dB)	38	25	0	-4.7~6.2	19–34	10	14.5–16
Reconfigurable Filter Shape	–	No	No	No	–	No	Yes
BW (MHz)	1–30	8	120–1500	9–15	2–76	15	20–40
NF (dB)	3.8–4.7	2.8	7.6–15.7	8.6	4.2–5.6	3.6–4.9	3.7–5.5
IIP3 (OOB) (dB)	10	26	–	17.5	12–14	36	25
Blocker P1dB (dBm)	-1	7	-1–4	14	>2	17	8.7
Area (w/ pads)	7.8	1.96	0.37	1.2	1.2	0.88	1.1
Power (mW)	76–96 ¹	18–57.4	112–125	75 ²	146.6–155	81–209	37.5–52.7

¹Excluding clock buffer power consumption

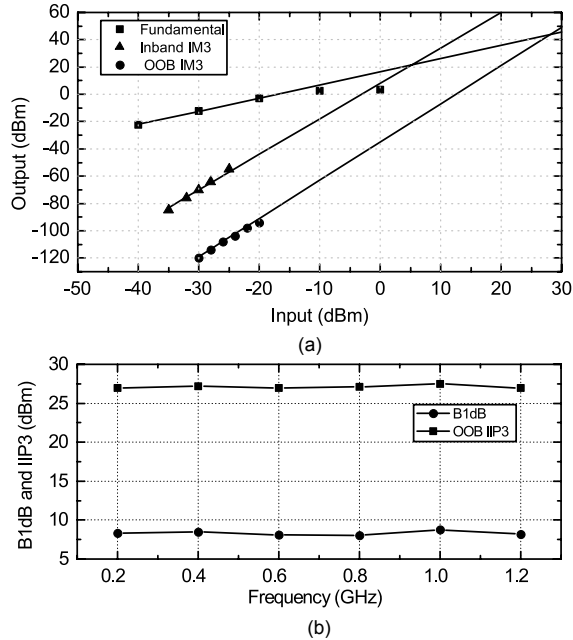
²At 700 MHz


Fig. 27. Measured non-linearity responses of the filter. (a) Out-of-band IIP3 and in-band IIP3 at 1 GHz. (b) Out-of-band IIP3 and blocker 1-dB compression point over the whole tuning range.

calculated using Thevenin and Norton equivalent circuits of the network as

$$-Y_{12} = \frac{I_{out}}{V'_{in}} = \frac{-y_{12} \cdot G_L}{y_{22} + G_L}, \quad (22)$$

and

$$G_{12} = \frac{V_{out}}{V'_{in}} = \frac{-y_{12}}{y_{22} + G_L}, \quad (23)$$

where $G_L = 1/R_L$. It is seen that for a normalized load resistance (i.e. $G_L = 1$ mho), $-Y_{12}$ and G_{12} can be found using the same expression as

$$H(s) = \frac{-y_{12}}{y_{22} + 1}. \quad (24)$$

This shows that the singly-terminated network can be described by its y_{12} and y_{22} . Therefore, the problem is reduced

to the simultaneous synthesis of y_{12} and y_{22} . It was shown that y_{12} and y_{22} are odd rational functions with the same denominator [22]. Therefore, they can be written as

$$y_{12}(s) = \frac{n_{12}(s)}{d_{22}(s)}, \quad (25)$$

and

$$y_{22}(s) = \frac{n_{22}(s)}{d_{22}(s)}, \quad (26)$$

where if $d_{22}(s)$ is an odd (even) polynomial, $n_{12}(s)$ and $n_{22}(s)$ are even (odd) polynomials. Inserting (25) and (26) back into (24) results in

$$H(s) = \frac{P(s)}{E(s)} = -\frac{n_{12}(s)}{n_{22}(s) + d_{22}(s)}. \quad (27)$$

Because the numerator and denominator of $H(s)$ are relatively prime, $P(s)$ can be found from the numerator of $y_{12}(s)$ and is either an odd or even polynomial. Similarly, $E(s)$ can be found from the sum of the numerator and the denominator of $y_{22}(s)$, and therefore is a Hurwitz polynomial. Therefore, the general form of the transfer function for the singly-terminated network in Fig. 5 is either

$$H(s) = \frac{P(s)}{E(s)} = \frac{M_1(s)}{M_2(s) + N_2(s)} = \frac{\frac{M_1(s)}{N_2(s)}}{\frac{M_2(s)}{N_2(s)} + 1}, \quad (28a)$$

or

$$H(s) = \frac{P(s)}{E(s)} = \frac{N_1(s)}{M_2(s) + N_2(s)} = \frac{\frac{N_1(s)}{M_2(s)}}{\frac{N_2(s)}{M_2(s)} + 1}, \quad (28b)$$

where $M_i(s)$ and $N_i(s)$ ($i = 1, 2$) are the even and odd polynomials, respectively and $M_i(s) + N_i(s)$ ($i = 1, 2$) is a Hurwitz polynomial.

A comparison of (28a) and (28b) with (24) yields the following identifications

$$y_{12}(s) = -\frac{M_1(s)}{N_2(s)}, \quad (29a)$$

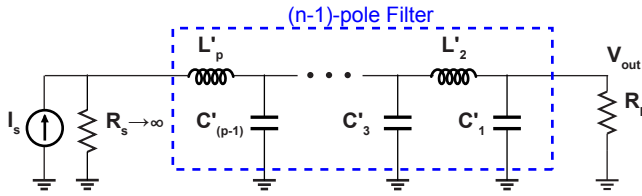


Fig. 28. Definition of the elements extracted from $y_{22}(s)$ in a singly-terminated lowpass filter.

and

$$y_{22}(s) = \frac{M_2(s)}{N_2(s)}, \quad (29b)$$

or

$$y_{12}(s) = -\frac{N_1(s)}{M_2(s)}, \quad (30a)$$

and

$$y_{22}(s) = \frac{N_2(s)}{M_2(s)}. \quad (30b)$$

Therefore, for realization of any arbitrary transfer function in the general form of (3b) as a singly-terminated network, it is required to decompose the denominator into odd and even polynomials and depending on the numerator being odd or even, divide both numerator and denominator to the even or odd portion of the denominator, respectively. This turns the transfer function into either (28a) or (28b). Then, the problem is reduced to simultaneous realization of y_{12} and y_{22} .

Because all transmission zeros in $H_2(s)$ lie at infinity, Cauer form-I (a ladder LC circuit with series inductors and shunt capacitors) is used to implement the circuit. Traditionally, a continued-fraction expansion of y_{22} is used to extract the elements of the network [31], although later other techniques have been developed. Among them, those involving *continuants* have received a lot of attention [32]–[34]. In [35], a recursive formula for extraction of element values for a general ladder network from a given input impedance or admittance function has been presented. To apply this method to (4b), it is written in a more general form of

$$y_{22}(s) = \frac{\sum_{i=0}^p a_i s^i}{\sum_{i=0}^q b_i s^i}, \quad (31)$$

where p is the order of the network to be synthesized (which is here $p = (n - 1)$) and therefore, it is an even integer number and also $p = q + 1$. Comparing (31) and (4b) reveals that not all $a_i s^i$ and $b_i s^i$ are available in (4b). Since element extraction reduces the order of polynomials successively, the level of reduction is tracked by using a superscript, while the subscript tracks the position of the element. Because the network is synthesized from the output port, the subscript is increased while moving toward the source, which is different from the convention used in Fig. 7. The element values, defined in Fig. 28, can be found from [35]

$$C'_{(2j-1)} = \frac{a_{(p-2j+2)}^j}{b_{(p-2j+1)}^j}, \quad (32a)$$

and

$$L'_{(2j)} = \frac{b_{(p-2j+1)}^j}{a_{(p-2j)}^{(j+1)}}, \quad (32b)$$

where $j = 1, 2, \dots, p/2$, and the initial values are found from

$$a_{(2i)}^j = a_{(2i)}^{(j-1)} - b_{(2i-1)}^{(j-1)} \frac{a_{(p-2j+4)}^{(j-1)}}{b_{(p-2j+3)}^{(j-1)}}, \quad (33a)$$

and

$$b_{(2i-1)}^j = b_{(2i-1)}^{(j-1)} - a_{(2i-2)}^j \frac{b_{(p-2j+3)}^{(j-1)}}{a_{(p-2j+2)}^j}, \quad (33b)$$

where $i = 1, 2, \dots, (p - 2j + 2)/2$ and $j \neq 1$.

When $j = 1$, the a_i^1 and b_i^1 are found from the coefficients of the polynomials in (31) as

$$a_i^1 = a_i \quad i = 1, 2, \dots, p, \quad (34a)$$

and

$$b_i^1 = b_i \quad i = 1, 2, \dots, q, \quad (34b)$$

and finally,

$$a_0^j = a_0 \quad j = 1, 2, \dots, (p/2) + 1, \quad (35a)$$

and

$$b_0^j = b_0 \quad j = 1, 2, \dots, p/2, \quad (35b)$$

which completes the element extraction procedure and hence, the synthesis method.

Now, as an example of how this recursive method can be used to synthesize a singly-terminated network, (32a) to (35b) are used to construct the circuit from $y_{22}(s)$ in (10b). The required calculations are as follows:

Step 1: From the polynomials in (10b), it is found that

$$p = 4, \quad q = 3,$$

$$a_0^1 = 1, \quad a_1^1 = 0, \quad a_2^1 = 3, \quad a_3^1 = 0, \quad a_4^1 = 1$$

$$b_0^1 = 0, \quad b_1^1 = 2.2360, \quad b_2^1 = 0, \quad b_3^1 = 2.2360.$$

also from (35a) and (35b), it can be found that

$$a_0^2 = a_0^2 = a_0^3 = 1,$$

$$b_0^1 = b_0^2 = 0.$$

Step 2: Then, (33a) and (33b) are used to find

$$a_2^2 = a_2^1 - b_1^1 \frac{a_4^1}{b_3^1} = 2,$$

$$b_1^2 = b_1^1 - a_0^2 \frac{b_3^1}{a_2^2} = 1.1180.$$

Step 3: finally, the elements values are found using (32a) and (32b) as

$$\begin{aligned} C'_1 &= a_4^1/b_3^1 = 0.4472 \text{ F}, \\ L'_2 &= b_3^1/a_2^2 = 1.1180 \text{ H}, \\ C'_3 &= a_2^2/b_1^2 = 1.7889 \text{ F}, \\ L'_4 &= b_1^2/a_0^3 = 1.1180 \text{ H}. \end{aligned}$$

APPENDIX II NON-LINEAR CIRCUIT ANALYSIS

In this section, a third order Taylor approximation of V_{out} versus V_{in} [36], [37] is derived. It is assumed that the second order non-linearity is negligible in fully differential configuration.

V_{out} is derived as a function of V_x, V_x^3 . From (16)

$$V_{out} = -\underbrace{\frac{g_{m2,1}}{g_{o2}}}_a V_x - \underbrace{\frac{g_{m2,3}}{g_{o2}}}_b V_x^3 - V_{out}^3 \quad (36)$$

$V_{out} = V_{out}(V_x, V_x^3)$: V_{out} is defined as: $V_{out} = \beta_1 V_x + \beta_3 V_x^3$, which is a 3rd order Taylor approximation around $V_x = 0$, where β_1, β_3 are the Taylor coefficients.

$$\beta_{n=1,2,3} = \frac{1}{n!} \left(\frac{\partial^n V_{out}}{\partial V_x^n} \right) \Big|_{V_x=0}$$

To derive β_1 , (36) is differentiated with respect to V_x as follows:

$$\begin{aligned} \frac{\partial V_{out}}{\partial V_x} &= a + 3bV_x^2 + 3V_{out}^2 \frac{\partial V_{out}}{\partial V_x} \\ &= \frac{a + 3bV_x^2}{1 - 3V_{out}^2} \end{aligned}$$

Taking derivative with respect to V_x again, it is found

$$\frac{\partial^2 V_{out}}{\partial^2 V_x} = \frac{6bV_x + 6V_{out} \left(\frac{\partial V_{out}}{\partial V_x} \right)^2}{1 - 3V_{out}^2}.$$

Also, the third derivative gives

$$\frac{\partial^3 V_{out}}{\partial^3 V_x} = \frac{6b + 6a^3 + 12cV_{out} \left(\frac{\partial V_{out}}{\partial V_x} \right)^2 + 6aV_{out} \frac{\partial^2 V_{out}}{\partial^2 V_x}}{1 - 3V_{out}^2}.$$

Therefore,

$$\begin{aligned} \beta_1 &= \left(\frac{\partial V_{out}}{\partial V_x} \right) \Big|_{V_x=0} = a = \frac{-g_{m2,1}}{g_{o2,1}} \\ \beta_2 &= \frac{1}{2} \left(\frac{\partial^2 V_{out}}{\partial V_x^2} \right) \Big|_{V_x=0} = 0 \\ \beta_3 &= \frac{1}{6} \left(\frac{\partial^3 V_{out}}{\partial V_x^3} \right) \Big|_{V_x=0} = b + a^3 c \end{aligned}$$

As a result, the output voltage

$$V_{out} = \underbrace{a}_{\beta_1} V_x + \underbrace{(b + a^3)}_{\beta_3} V_x^3 \quad (37)$$

$V_x = V_x(V_{out}, V_{out}^3)$: It is possible to write the inverse of (37) in the Taylor series form: $V_x = \alpha_1 V_{out} + \alpha_3 V_{out}^3$, where α_1, α_3 are the Taylor coefficients.

$$\begin{aligned} V_x &= \alpha_1 V_{out} + \alpha_3 V_{out}^3 \\ &= \alpha_1 (\beta_1 V_x + \beta_3 V_x^3) + \alpha_3 (\beta_1 V_x + \beta_3 V_x^3)^3 \\ &= \alpha_1 \beta_1 V_x + \alpha_1 \beta_3 V_x^3 + \alpha_3 \beta_1 V_x^3 + \dots \end{aligned}$$

Equating the terms on both sides

$$\begin{aligned} \alpha_1 &= \frac{1}{a} \\ \alpha_3 &= -\frac{b + a^3}{a^4} \end{aligned}$$

$$V_x = \underbrace{\frac{1}{a}}_{\alpha_1} V_{out} - \underbrace{\frac{(b + a^3 c)}{a^4}}_{\alpha_3} V_{out}^3 \quad (38)$$

The output current of first g_m cell

$$I_s = -g_{m1,1} V_{in} - g_{m1,3} V_{in}^3 \quad (39)$$

Now, from Fig. 18, it is possible to write

$$\begin{aligned} I_s &= I_o + I_F = \frac{V_x}{r'_{o1}} - g_{m3,1} V_{out} - g_{m3,3} V_{out}^3 \\ &= V_{out} \left(-g_{m3,1} + \frac{1}{ar'_{o1}} \right) - \left(\frac{b + a^3 c}{a^4 r'_{o1}} + g_{m3,3} \right) V_{out}^3 \end{aligned} \quad (40)$$

Equating (39) and (40), yields

$$\begin{aligned} V_{out} &= \frac{g_{m1,1}}{g_{m3,1} - \frac{1}{ar'_{o1}}} V_{in} + \frac{g_{m1,3}}{g_{m3,3} - \frac{1}{ar'_{o1}}} V_{in}^3 + p V_{out}^3 \\ &= m V_{in} + n V_{in}^3 + p V_{out}^3 \end{aligned} \quad (41)$$

where $p = \frac{b + a^3 c + a^4 g_{m3,3} r'_{o1}}{a^4 r'_{o1} \left(\frac{1}{ar'_{o1}} - g_{m3,1} \right)}$.

Therefore,

$$\frac{\partial V_{out}}{\partial V_{in}} = m + 3n V_{in}^2 + 3p V_{out}^2 \frac{\partial V_{out}}{\partial V_{in}} \quad (42)$$

By using the same procedure above, it is found that

$$\begin{aligned} V_{out} &= m V_{in} + (n + m^3 p) V_{in}^3 \\ &= \frac{g_{m1,1}}{g_{m3,1} + \frac{1}{g_{m2,1} r'_{o1} r'_{o2}}} V_{in} + T V_{in}^3 \end{aligned} \quad (43)$$

where

$$T = \frac{g_{m1,3}}{g_{m3,3} + \frac{1}{g_{m2,1} r'_{o1} r'_{o2}}} + \left(\frac{g_{m1,1}}{g_{m3,1} + \frac{1}{g_{m2,1} r'_{o1} r'_{o2}}} \right)^3 \times p.$$

REFERENCES

- [1] "3GPP TS 36.300 v 12.6.0, June 2015; technical specification group radio access network; evolved universal terrestrial radio access (E-UTRA) and evolved universal terrestrial radio access network (E-UTRAN); overall description; stage 2, release 11."
- [2] R. Chen and H. Hashemi, "Reconfigurable receiver with radio-frequency current-mode complex signal processing supporting carrier aggregation," *IEEE Journal of Solid-State Circuits*, vol. 50, no. 12, pp. 3032–3046, Dec. 2015.
- [3] Y. Xu and P. R. Kinget, "A switched-capacitor RF front end with embedded programmable high-order filtering," *IEEE Journal of Solid-State Circuits*, vol. 51, no. 5, pp. 1154–1167, May 2016.
- [4] D. Yang, H. Yüksel, and A. Molnar, "A wideband highly integrated and widely tunable transceiver for in-band full-duplex communication," *IEEE Journal of Solid-State Circuits*, vol. 50, no. 5, pp. 1189–1202, May 2015.
- [5] M. N. Hasan, Q. J. Gu, and X. Liu, "Tunable blocker-tolerant on-chip radio frequency front-end filter with dual adaptive transmission zeros for software defined radio applications," *IEEE Transactions on Microwave Theory and Techniques*, vol. 64, no. 12, Dec 2016.
- [6] R. Chen and H. Hashemi, "Passive coupled-switched-capacitor-resonator-based reconfigurable RF front-end filters and duplexers," in *Proc. IEEE Radio Frequency Integrated Circuits Symp. (RFIC)*, May 2016, pp. 138–141.
- [7] N. Reiskarimian and H. Krishnaswamy, "Design of all-passive higher-order cmos n-path filters," in *Radio Frequency Integrated Circuits Symposium (RFIC), 2015 IEEE*. IEEE, 2015, pp. 83–86.
- [8] M. Darvishi, R. Van der Zee, and B. Nauta, "Design of active N-path filters," *IEEE Journal of Solid-State Circuits*, vol. 48, no. 12, pp. 2962–2976, Dec 2013.
- [9] C.-K. Luo, P. S. Gudem, and J. F. Buckwalter, "A 0.2–3.6-GHz 10-dBm B1dB 29-dBm IIP3 Tunable filter for transmit leakage suppression in SAW-less 3G/4G FDD receivers," *IEEE Transactions on Microwave Theory and Techniques*, vol. 63, no. 10, pp. 3514–3524, 2015.
- [10] R. Chen and H. Hashemi, "Dual-carrier aggregation receiver with reconfigurable front-end rf signal conditioning," *IEEE Journal of Solid-State Circuits*, vol. 50, no. 8, pp. 1874–1888, 2015.
- [11] M. N. Hasan, Q. Gu, and X. Liu, "Reconfigurable blocker-tolerant RF front-end filter with tunable notch for active cancellation of transmitter leakage in FDD receivers," *International Symposium on Circuits and Systems (ISCAS)*, pp. 1782–1785, May 2016.
- [12] A. Ghaffari, E. Klumperink, M. C. M. Soer, and B. Nauta, "Tunable high-Q N-path band-pass filters: Modeling and verification," *IEEE Journal of Solid-State Circuits*, vol. 46, no. 5, pp. 998–1010, 2011.
- [13] A. Ghaffari, E. Klumperink, and B. Nauta, "Tunable N-path notch filters for blocker suppression: Modeling and verification," *IEEE Journal of Solid-State Circuits*, vol. 48, no. 6, pp. 1370–1382, 2013.
- [14] M. N. Hasan, Q. Gu, and X. Liu, "Tunable blocker-tolerant RF front-end filter with dual adaptive notches for reconfigurable receivers," in *2016 IEEE MTT-S International Microwave Symposium (IMS)*, May 2016, pp. 1–4.
- [15] C. Andrews and A. C. Molnar, "A passive mixer-first receiver with digitally controlled and widely tunable RF interface," *IEEE Journal of Solid-State Circuits*, vol. 45, no. 12, pp. 2696–2708, Dec. 2010.
- [16] C. Andrews and A. C. Molnar, "Implications of passive mixer transparency for impedance matching and noise figure in passive mixer-first receivers," *IEEE Transactions on Circuits and Systems I: Regular Papers*, vol. 57, no. 12, pp. 3092–3103, Dec. 2010.
- [17] R. Chen and H. Hashemi, "Reconfigurable blocker-resilient receiver with concurrent dual-band carrier aggregation," in *2014 IEEE Proceedings of the Custom Integrated Circuits Conference (CICC)*, 2014, pp. 1–4.
- [18] A. Mirzaei and H. Darabi, "Analysis of imperfections on performance of 4-phase passive-mixer-based high-q bandpass filters in SAW-less receivers," *IEEE Transactions on Circuits and Systems I: Regular Papers*, vol. 58, no. 5, pp. 879–892, May 2011.
- [19] G. Agrawal, S. Aniruddhan, and R. K. Ganti, "A compact mixer-first receiver with >24 dB self-interference cancellation for full-duplex radios," *IEEE Microwave and Wireless Components Letters*, vol. 26, no. 12, pp. 1005–1007, Dec. 2016.
- [20] N. Reiskarimian, M. B. Dastjerdi, J. Zhou, and H. Krishnaswamy, "Highly-linear integrated magnetic-free circulator-receiver for full-duplex wireless," in *Proc. IEEE Int. Solid-State Circuits Conf. (ISSCC)*, Feb. 2017, pp. 316–317.
- [21] G. L. Matthaei, L. Young, and E. Jones, *Microwave filters, impedance-matching networks, and coupling structures*. Dedham, MA, USA: Artech house, 1980.
- [22] R. J. Cameron, C. M. Kudsia, and R. R. Mansour, *Microwave Filters for Communication Systems: Fundamentals, Design and Applications*. New York, NY, USA: Wiley-Interscience, 2007.
- [23] S. Saeedi, J. Lee, and H. H. Sigmarsson, "A new property of maximally-flat lowpass filter prototype coefficients with application in dissipative loss calculations," *Progress In Electromagnetics Research C*, vol. 63, pp. 1–11, 2016.
- [24] D. M. Pozar, *Microwave Engineering, 4th Edition*. Danvers, MA, USA: John Wiley & Sons, Inc., 2011.
- [25] H. Joshi, H. H. Sigmarsson, S. Moon, D. Peroulis, and W. J. Chappell, "High-Q fully reconfigurable tunable bandpass filters," *IEEE transactions on microwave theory and techniques*, vol. 57, no. 12, pp. 3525–3533, 2009.
- [26] E. J. Naglich, J. Lee, D. Peroulis, and W. J. Chappell, "A tunable bandpass-to-bandstop reconfigurable filter with independent bandwidths and tunable response shape," *IEEE Transactions on Microwave Theory and Techniques*, vol. 58, no. 12, pp. 3770–3779, 2010.
- [27] S. Saeedi, J. Lee, and H. H. Sigmarsson, "Tunable, high-Q, substrate-integrated, evanescent-mode cavity bandpass-bandstop filter cascade," *IEEE Microwave and Wireless Components Letters*, vol. 26, no. 4, pp. 240–242, 2016.
- [28] M. Hasan, S. Aggarwal, Q. Gu, and X. Liu, "Tunable N-path RF front-end filter with an adaptive integrated notch for FDD/co-existence," in *2015 IEEE International Midwest Symposium on Circuits and Systems (MWSCAS)*, 2015, pp. 1–4.
- [29] F. Amin, S. Raman, and K. J. Koh, "A high dynamic range 4th-order 4–8 GHz Q-enhanced LC band-pass filter with 2–25% tunable fractional bandwidth," in *2016 IEEE MTT-S International Microwave Symposium (IMS)*, May 2016, pp. 1–4.
- [30] C.-K. Luo, P. S. Gudem, and J. F. Buckwalter, "A 0.4–6-GHz 17-dBm B1dB 36-dBm IIP3 channel-selecting low-noise amplifier for SAW-less 3G/4G FDD diversity receivers," *IEEE Transactions on Microwave Theory and Techniques*, vol. 64, no. 4, pp. 1110–1121, 2016.
- [31] M. E. Van Valkenburg, *Introduction to modern network synthesis*. New York, NY, USA : Wiley, 1965.
- [32] H. Orchard, "Some explicit formulas for the components in low-pass ladder networks," *IEEE Trans. Circuit Theory*, vol. 17, no. 4, pp. 612–616, 1970.
- [33] P. Mariotto, "On the explicit formulas for the elements in low-pass ladder filters," *IEEE Trans. Circuits Syst.*, vol. 37, no. 11, pp. 1429–1436, 1990.
- [34] R. Gudipati and W.-K. Chen, "Explicit formulas for element values of the lowpass, highpass and bandpass ladders with Butterworth or Chebyshev response," in *1993 IEEE International Midwest Symposium on Circuits and Systems (MWSCAS)*, 1993, pp. 645–648.
- [35] R. Gudipati and W.-K. Chen, "Explicit formulae for element values of a lossless low-pass ladder network and their use in the design of a broadband matching network," *Journal of the Franklin Institute*, vol. 326, no. 2, pp. 167–184, 1989.
- [36] B. Razavi, *RF Microelectronics*, 2nd ed. Upper Saddle River, NJ, USA: Prentice Hall Press, 2011.
- [37] D. H. Mahrof, E. A. Klumperink, Z. Ru, M. S. Oude Alink, and B. Nauta, "Cancellation of opAmp virtual ground imperfections by a negative conductance applied to improve RF receiver linearity," *IEEE Journal of Solid-State Circuits*, vol. 49, no. 5, pp. 1112–1124, 2014.